Journal of Materials Chemistry C

PAPER

Check for updates

A novel approach of an infrared transparent Er:Y$_2$O$_3$–MgO nanocomposite for eye-safe laser ceramics†

Ho Jin Ma, Wook Ki Jung, Youngtae Park and Do Kyung Kim ⓘD *

Er^{3+} ion doped eye-safe lasers operating at a wavelength of 1.5 μm have attracted attention for use in many applications requiring protection from accidental retina exposure. For eye-safe lasers, it is considered important to improve the thermal and mechanical stability of the host materials for high power operation. Transparent Y$_2$O$_3$ is the most representative example among different types of host materials due to its low maximum phonon energy. However, this host shows low thermal conductivity with increasing dopant concentration. Herein, we prepare an Er:Y$_2$O$_3$–MgO nanocomposite as a new host material candidate that shows excellent optical, mechanical and thermal properties. By limiting domain coalescence and eliminating residual pores during sintering, outstanding optical transmittance is demonstrated for the Er:Y$_2$O$_3$–MgO nanocomposite. We also investigated the fluorescence spectrum and cross-section values to evaluate the possibility of using the Y$_2$O$_3$–MgO nanocomposite as a laser gain medium. The Er:Y$_2$O$_3$–MgO nano-composite also shows excellent mechanical and thermal properties at high Er^{3+} ion dopant concentrations. The results indicate that Y$_2$O$_3$–MgO nanocomposite ceramics are promising candidate materials for use as high-power infrared laser hosts.

1. Introduction

High-energy eye-safe lasers have been developed over several decades for use in many fields of application requiring both increased power output and protection against inevitable exposure to humans. An eye-safe laser is attractive for applications in multi-dimensional scanning, wind detection and autonomous vehicle LIDAR, time-resolved spectroscopy, optical communications and medical applications.[1–4] Nowadays, with increasing beam power, it is essential to develop the means to protect human eyes from intense laser pulses. Unnecessary eye hazards can be prevented by either adopting optical power limiting (OPL) materials[5–7] or selecting appropriate activator ions, which emit near-infrared wavelength light. Especially, wavelengths longer than 1.4 μm are strongly absorbed by ocular components including the cornea, vitreous and aqueous humor, which can reduce light transmission before it reaches the retina.[2] In addition, there is a high atmospheric transmission window in this wavelength region that minimizes power loss. For eye-safe lasers, Er^{3+} ions have been used as the activator, which show a 4f intermanifold

transition (^{4}I$_{15/2}$ → ^{4}I$_{13/2}$) at 1.5 μm, which can be used to operate a resonantly pumped laser.[8,9] The use of Er^{3+} ions is also favorable for cascade excitation due to the small non-radiative transition probabilities with large numbers of energy level channels, which improve the emission efficiency.[10,11] Therefore, Er^{3+} ions have been widely doped into a variety of host materials including glass, single crystal and polycrystalline ceramics for eye-safe laser applications.

As promising host materials, solid-state laser ceramics have been extensively studied for use as substitutes for single-crystal laser media with Dy:CaF$_2$ materials.[12] The polycrystalline ceramics show many advantages for high-power laser applications including large-scale fabrication, geometric versatility, and high and homogeneous doping without segregation of dopant ions.[13] The sought-after polycrystalline hosts are Y$_3$Al$_5$O$_{12}$ (YAG) and the sesquioxides including Y$_2$O$_3$, Sc$_2$O$_3$ and Lu$_2$O$_3$. In particular, the sesquioxides show high thermal conductivity, chemical stability, and emission cross-section compared to YAG.[14–16] Y$_2$O$_3$ has a low maximum phonon energy (∼590 cm^{-1}) that can alleviate multi-phonon relaxation.[17] When increasing the dopant concentration in Y$_2$O$_3$, however, the thermal and mechanical stress inevitably increase during high power laser operation, which is an intrinsic drawback for the host material. To reduce thermal lensing effects and facilitate heat dissipation in host materials, many studies have demonstrated improvements in the design of the gain medium by fabricating multilayer

Department of Materials Science and Engineering, Korea Advanced Institute of Science and Technology (KAIST), Daejeon 305-701, Republic of Korea.
E-mail: dkkim@kaist.ac.kr

and clad–core composites with a graded doping concentration.[13,18] Compared to polycrystalline ceramics with a uniform concentration of dopants, the graded dopant profile provides enhanced thermal distribution during high-power operation.[13] While such a composite can be used to alleviate thermal problems for the gain medium, the preparation of a gain medium with a varying doping profile involving additional bonding processes is required.

To overcome the drawbacks in the fabrication and intrinsic characterization of the gain medium properties including mechanical and thermal properties, we designed an Y_2O_3–MgO nanocomposite as an eye-safe laser-host material based on a simple fabrication process. Unlike the Y_2O_3 single phase, the MgO phase can effectually prohibit grain coarsening in the Y_2O_3 phase through the Zener pinning effect.[19,20] Although this limits the transparency in the visible region due to the difference in the refractive index between two phases, the reduced grain size improves the mechanical properties and near-infrared transmittance of the host. Furthermore, the thermal conductivity is also enhanced since the MgO phase plays a vital role in the thermal transport.[17,21] Based on this approach, we have recently reported the influence of having a well controlled microstructure for an Y_2O_3–MgO nanocomposite on the optical and mechanical properties.[22] However, there have been no reports on the spectroscopic, thermal, and mechanical properties of the Er:Y_2O_3–MgO nanocomposite for eye-safe laser operation despite the significant potential for exploitation in high-power applications.

Here, we report a simple design for an eye-safe laser gain medium that utilizes Er^{3+} ions doped into a Y_2O_3–MgO nanocomposite to enhance the thermomechanical properties, and which exhibits fluorescence at 1.5 μm. Polycrystalline Er:Y_2O_3–MgO ceramics with different doping concentrations are synthesized by a glycine–nitrate process followed by direct sintering of particles by a hot-press method. We achieved an excellent infrared transmittance due to the elimination of residual pores and the prevention of grain growth during the sintering process. The photoluminescence, absorption, emission and gain cross-section of the Er:Y_2O_3–MgO nanocomposite are measured. Moreover, we demonstrate improved mechanical and thermal properties of the Er:Y_2O_3–MgO nanocomposite with high incorporation of the Er^{3+} ions, which is promising in the context of potential applications for the host materials.

2. Experimental section

2.1 Synthesis and sintering of the Er:Y_2O_3–MgO nanocomposite

Er:Y_2O_3–MgO nanocomposite ceramics with 50:50 volume fractions were fabricated by the glycine nitrate process (GNP) and hot-press sintering method. Yttrium nitrate hexahydrate (Y(NO$_3$)·6H$_2$O, ≥99.8%, Sigma Aldrich), magnesium nitrate hexahydrate (Mg(NO$_3$)$_2$·6H$_2$O, ≥99%, Sigma Aldrich), erbium nitrate hexahydrate (Er(NO$_3$)$_3$·6H$_2$O, ≥99.9%, Sigma Aldrich) and glycine (NH$_2$CH$_2$COOH, ≥99%, Sigma Aldrich) were used as starting chemicals for the nanopowder synthesis. The raw materials were dissolved in distilled water. The stoichiometric

molar ratio of nitrate-to-glycine (N/G) used corresponded to 0.75, with the erbium doping concentration varied from 0 to 10 at%. The solution was placed onto a heating mantle, and then heated for a few minutes. Following the self-ignition reaction, the as-synthesized voluminous particles were ball milled using ZrO_2 media in ethyl alcohol for 24 hours. The mixed slurry was then dried before calcination at 800 °C for 5 hours in a box furnace.

The calcined Er:Y_2O_3–MgO nanoparticles were sieved through a 200-mesh, and then sintered *via* the hot-pressing method. The specimens were heated to 1300 °C using a heating rate of 15 °C min^{-1} under an Ar atmosphere. The samples were maintained at this temperature for 1 hour at 50 MPa before being cooled down at 5 °C min^{-1}. To eliminate oxygen vacancies and residual carbon, a post-annealing process was carried out at 1150 °C for 10 hours in air. The annealed samples were then mirror-polished to enable observation of the optical performance. A 5 at% Er^{3+} ion doped Y_2O_3 polycrystalline host was also prepared for comparison of the absorption patterns. Er:Y_2O_3 particles were synthesized by the GNP method, using the same stoichiometric ratio and processing used for Er:Y_2O_3–MgO, followed by sintering at 1450 °C for 1 hour at 50 MPa.

2.2 Characterization of the Er:Y_2O_3–MgO nanocomposite

Powders were characterized by using a conventional powder X-ray diffraction (XRD) technique with CuKα radiation at room temperature at a scan rate of 5° min^{-1} between 15 and 80° (SmartLab, Rigaku). The particle images were obtained using Scanning Electron Microscopy (SEM, Model Philips XL 30 FEG, Philips). The morphology and lattice were examined by using transmittance electron microscopy (TEM) *via* the generation of selected area electron diffraction (SAED) patterns and fast Fourier transform (FFT) images (Tecnai G2F30 S-Twin, FEI). Thermogravimetric analysis and differential scanning calorimetry (TGA-DSC) analysis of the as-synthesized nanocomposite particles were carried out at temperatures ranging from room temperature to 1000 °C in an air atmosphere (LABSYS Evo, Setaram). The heating rate was 10 °C min^{-1}. After hot-pressing, the sample density was measured by the Archimedes method. The pellets were thermally etched at 1100 °C for 2 hours before taking microstructure images using the SEM equipment (Model Philips XL 30 FEG, Philips). UV-Vis/NIR spectra were used to measure the transmittance and absorbance in a wavelength range of 200–3000 nm (Lambda 1050, PerkinElmer). Photoluminescence (PL) spectra were recorded using excitation by a 450 W xenon source at 975 nm at room temperature (Fluorolog3, Horiba Scientific). The photoexcitation monochromator was equipped with a 1200 grooves per mm grating blazed at 500 nm. An InGaAs detector with LN cooler was used for measuring light emission originating from the $^4I_{13/2} \rightarrow {}^4I_{15/2}$ transition. The Vickers hardness was measured using a Vickers hardness tester (VLPAK2000, Mitutoyo) with a load of 1 kgf placed on the mirror-polished surface. For measurement of the fracture toughness, imprints and cracks caused by the Vickers indentation were measured using SEM. The thermal conductivity of the nanocomposite ceramics was calculated from the measured specific heat, thermal diffusivity and density at room temperature.

This journal is © The Royal Society of Chemistry 2018

J. Mater. Chem. C, 2018, **6**, 11096–11103 | 11097

The heat capacity was determined by differential scanning calorimetry (Model DSC 204 F1, Netzsch). The thermal diffusivity was determined using the laser flash method (LFA 467, Netzsch).

3. Results and discussion

To confirm the crystal structure and phase purity of a series of synthesized Er:Y_2O_3–MgO nanoparticles with different doping concentrations, X-ray diffraction (XRD) analysis was carried out. As shown in Fig. 1(a), the observed X-ray diffraction peaks are consistent with the peaks expected for the cubic Y_2O_3 (JCPDS No. 72-0927) and MgO (JCPDS No. 74-1225) phases. The data indicate a complete synthesis of the Y_2O_3–MgO nanopowder through a single reaction process without impurity phases including Er_2O_3. It is noteworthy that the Y_2O_3 peaks shift to a slightly higher diffraction angle when the Er^{3+} ion doping concentration increases, implying a decrease in the lattice parameters and unit cell volume. The lattice constants calculated from the diffraction patterns for both Y_2O_3 and MgO phases as a function of Er^{3+} concentration are shown in Fig. 1(b). As the Er^{3+} ion concentration is increased to 10 at%, the lattice parameter of Y_2O_3 is reduced from 10.60 to 10.58. This is because the Er^{3+}(89 pm) ions, having a smaller ionic radius, substitute for the Y^{3+}(90 pm) ions despite the small difference in the radii of the two ions.[23] On the other hand, since the MgO phase is not affected by the incorporation of Er^{3+} ions during the synthesis, the corresponding values for the MgO phase are consistent. Based on these results, the MgO phase can be expected to influence only the heat transfer during the laser operation but not the fluorescence.

A scanning electron microscopy (SEM) image of the as-synthesized 5 at% Er:Y_2O_3–MgO nanoparticles calcined at 800 °C is shown in Fig. 1(c). It can be seen that agglomerated particles are formed for the nanocomposite powders synthesized via the glycine–nitrate process. Spontaneous exothermic reaction enables the formation of fine particles with a large specific surface area, which induces agglomeration followed by calcination.[24,25] The morphology and crystallinity of the as-synthesized 5 at% Er:Y_2O_3–MgO nanoparticles were evaluated by transmission electron microscopy (TEM) and selected-area electron diffraction (SAED) patterns. As shown in Fig. 1(d), both the Er:Y_2O_3 and MgO phases are homogeneously distributed, with an average particle size of less than 20 nm after calcination. Based on the SAED analysis in Fig. 1(e), the indexed diffraction patterns reveal a cubic crystal structure for Y_2O_3 as well as MgO, consistent with the X-ray data shown in Fig. 1(a). It is clear that both Y_2O_3 and MgO nanoparticles are well crystallized. The lattice distances of the synthesized Y_2O_3 and MgO nanoparticles can be also calculated from the FFT patterns given in Fig. 1(f and g). The distances were found to be 0.211 and 0.433 nm, corresponding to the (200) plane of cubic MgO and (211) plane of cubic Y_2O_3.

Fig. S1 of the ESI† shows the TGA-DSC curves of the as-synthesized nanocomposite particles. It is apparent that there is a large weight loss in the TG curve. In the early stage, the adsorbed water in the synthesized particles evaporates below 200 °C. Then, the weight loss from 287 °C is attributed to the crystallization, elimination of gas phases and decomposition of residues. The temperature of the decomposition reaction in the TGA curve corresponds to the sharp exothermal peak in the DSC curve. The total weight loss of the as-synthesized particles is 17.8% up to 1000 °C.

A hot-press method was used for consolidation of the Er:Y_2O_3–MgO nanocomposite ceramics. Sintering was carried out at 1300 °C for 1 hour at 50 MPa in an Ar atmosphere. Following the sintering process, all samples were post-annealed in the air to eliminate oxygen vacancies and residual lattice stress. The microstructure images of the nanocomposites with different doping concentrations are shown in Fig. 2(a–f). The data show no apparent difference in the porosity and grain size for the nanocomposite as a function of the doping concentration. Since the fine particles synthesized by the GNP method show excellent sinterability with a short mass-transfer distance, evidence of residual intergranular pores was not observed in any of the samples. Grain coarsening of the nanocomposite can be effectively restricted during the sintering process because of both the use of the hot-press method and the Zener pinning effect between the Er:Y_2O_3 and MgO phases, which can mutually prohibit mass transport.[19] The density and average grain size of the nanocomposite with different doping concentrations are represented in Fig. 2(g). The density of the nanocomposite increases from 4.26 to 4.41 g cm^{-3} with increasing concentration of Er^{3+} ions from 0.5 to 10 at%. This is likely due to substitution of the Y^{3+} ions for the heavier Er^{3+} ions. In contrast, no difference is observed for the average grain size as a function of Er^{3+} doping concentration, with the
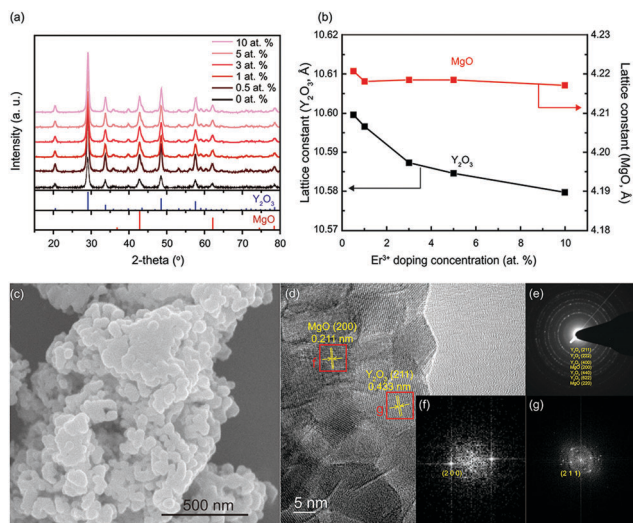
Fig. 1 (a) X-ray diffraction patterns of the as-synthesized Er:Y_2O_3–MgO nanopowders with varying Er^{3+} ions doping concentrations from 0.5 to 10 at%. (b) Lattice parameters of the Y_2O_3 and MgO phases with varying Er^{3+} ion doping concentrations. (c) SEM and (d) HRTEM images of the as-synthesized 5 at% Er:Y_2O_3–MgO nanoparticles after calcination at 800 °C for 5 hours in air. (e) SAED patterns of 5 at% Er:Y_2O_3–MgO nanoparticles. Fast Fourier Transform (FFT) patterns of the selected area marked (f) 'f' and (g) 'g' in (d).

11098 | J. Mater. Chem. C, 2018, 6, 11096–11103

This journal is © The Royal Society of Chemistry 2018
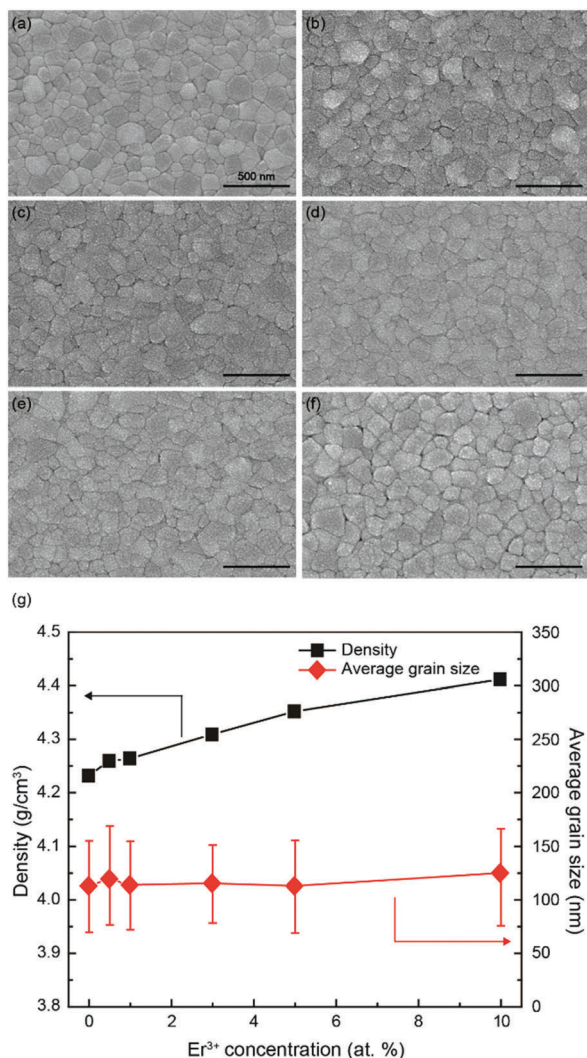
Fig. 2 SEM microstructure images of an Er:Y_2O_3–MgO nanocomposite taken after hot-pressing at 1300 °C for 1 hour in an Ar atmosphere. The Er^{3+} doping concentrations of the samples are: (a) 0, (b) 0.5, (c) 1, (d) 3, (e) 5, and (f) 10 at%; (g) the density and average grain size of the sintered samples at 1300 °C with different varying Er^{3+} ion doping concentrations.

measured values ranging between 110 and 120 nm. The substitution of Er^{3+} for Y^{3+} ions does not have an influence on the grain growth because of the similar ionic radii of Er^{3+} and Y^{3+} ions. This result differs from that obtained for the well-known Nd:Y_2O_3 transparent ceramic. For this material, there is a large difference in the ionic radii of Nd^{3+} and Y^{3+} that results in lattice distortion, which accelerates the mass transport and grain growth.[26] Therefore, it is clear that by limiting domain growth, the Er:Y_2O_3–MgO nanocomposite ceramics can demonstrate excellent mechanical properties for high output laser operation despite the incorporation of a high concentration of Er^{3+} ions.

The near-infrared in-line transmittance of the Er:Y_2O_3–MgO nanocomposite with different doping concentrations is shown in Fig. 3(a). In all nanocomposite samples, a high transmittance of up to 80% can be obtained in the mid-infrared wavelength region.
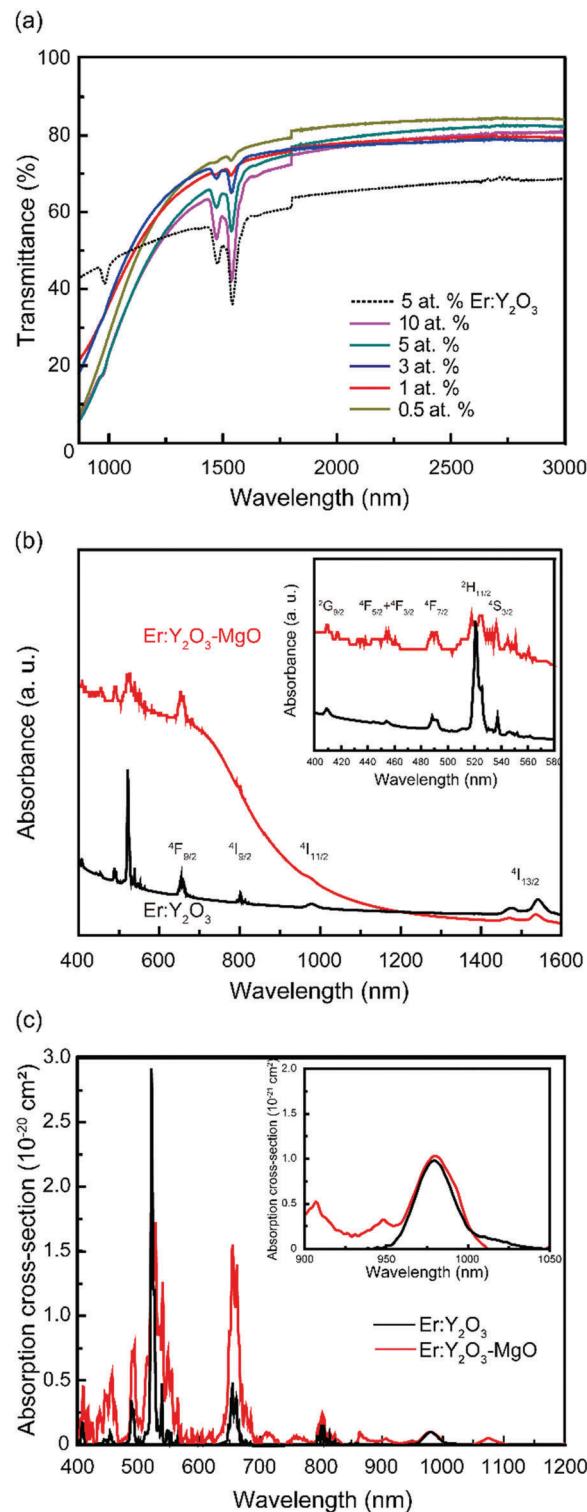
Fig. 3 (a) Infrared transmittance of a sintered Er:Y_2O_3–MgO nanocomposite with varying doping concentrations from 0.5 to 10 at% and 5 at% Er:Y_2O_3. (b) Absorbance spectra of 5 at% Er:Y_2O_3–MgO and Er:Y_2O_3 transparent ceramics. The inset shows the absorbance measured in the visible region. (c) Absorption cross-sections of 5 at% Er:Y_2O_3–MgO and Er:Y_2O_3 ceramics. The inset shows the absorption cross-section in the NIR region.

This journal is © The Royal Society of Chemistry 2018

J. Mater. Chem. C, 2018, 6, 11096–11103 | 11099

As shown by the observed microstructure, well-distributed fine particles and the use of the hot-press method can induce outstanding sinterability of the Er:Y_2O_3–MgO nanocomposite, resulting in sufficient elimination of the residual pores. On the other hand, the optical performance of the Er:Y_2O_3–MgO nanocomposite decreased in the visible region due to grain boundary scattering induced by the relatively large difference in the refractive index between the Y_2O_3 and MgO phases. Therefore, the Y_2O_3–MgO nanocomposite cannot be used in visible light laser applications. However, it can be applied as an infrared laser gain medium by using Er^{3+} or Ho^{3+} ions as activators. The transmittance of the 5 at% Er^{3+} ion doped Y_2O_3 ceramics sintered via the hot-press method is also (see dashed line) compared with the absorption bands observed for the Er:Y_2O_3–MgO nanocomposite. The transparency in the mid-infrared region of 5 at% Er:Y_2O_3 is much lower than that of the Er:Y_2O_3–MgO nanocomposite because the sintering conditions are insufficient to obtain a highly dense ceramic. In general, Y_2O_3 transparent ceramics are consolidated above 1700 °C for 5–20 hours under H_2 or vacuum conditions.[27,28] The sintering process used in this study retains the residual pores, which contributes to the degradation in the transparency. While there is a difference in the transmittance between Er:Y_2O_3 and Er:Y_2O_3–MgO transparent ceramics, the positions of the intense absorption peaks remain the same. There is no shift in the position of the absorption bands at 1.54 and 0.98 μm regardless of the different doping concentrations and the presence of MgO phases. The absorption peaks of 5 at% doped Er:Y_2O_3 and the Er:Y_2O_3–MgO nanocomposite measured in the wavelength region of 400–1600 nm at room temperature are shown in Fig. 3(b). The data clearly show a broad absorbance for Er:Y_2O_3–MgO in the visible region due to grain boundary scattering. The absorption peaks of the Er:Y_2O_3–MgO nanocomposite in the visible and near-infrared regions follow those observed for the Er:Y_2O_3 ceramics despite the intrinsic absorption band. It is apparent that several absorption bands corresponding to the transitions from ground state to $^4I_{13/2}$, $^4I_{11/2}$, $^4I_{9/2}$, $^4F_{9/2}$, $^4S_{3/2}$, $^2H_{11/2}$, $^4F_{7/2}$, $^4F_{5/2} + ^4F_{3/2}$ and $^2G_{9/2}$, including the multiplet manifolds $^{2S+1}L_j$, can be observed for both Er:Y_2O_3–MgO and Er:Y_2O_3 ceramics. The absorption peaks are in agreement with those previously reported for the Er^{3+} ion in the C_2 sites of the Y_2O_3 host material.[29] The absorption cross-section of both 5 at% Er:Y_2O_3–MgO and Er:Y_2O_3 ceramics for the visible and NIR region (inset) are shown in Fig. 3(c). The values are derived from the normalized absorption coefficient correcting for surface reflection and scattering factors.[30,31] As mentioned above, the transition levels of Er:Y_2O_3–MgO coincide with the values of Er:Y_2O_3 in the visible and NIR wavelength region. The calculated absorption cross-section of the Er:Y_2O_3–MgO nanocomposite shows similar results compared with previous studies of Er:Y_2O_3 transparent ceramics.[32,33] In this study, the absorption cross-section of Er:Y_2O_3–MgO is similar to the value of Er:Y_2O_3 at 975 nm. The results show that Er:Y_2O_3–MgO can be efficiently pumped at visible and NIR wavelengths below 1000 nm for infrared laser oscillation.

The room temperature photoluminescence spectra of the Er:Y_2O_3–MgO nanocomposite with a varying doping concentration

were recorded. As can be observed in Fig. 4(a), under 975 nm CW xenon lamp excitation, multiple intense Er^{3+} ion emission bands are evident from 1400 to 1700 nm, which are assigned to the $^4I_{13/2}$ and $^4I_{15/2}$ Stark splitting.[29,34] For all samples, no shift in the emission peaks or broadening was observed for varying dopant concentrations, which indicates that the erbium doping concentration does not induce radiation trapping effects, providing collateral emission bands.[35] It is clear that the strongest emission peak intensity for the Er:Y_2O_3–MgO nanocomposite occurred at 1535 nm. As shown in Fig. 4(b), while the peak intensity at approximately 1535 nm increases gradually with increasing doping concentration to 5 at%, it decreases with a further increase in the doping concentration to 10 at% due to concentration quenching. Such concentration quenching results from cross-relaxation interactions with non-radiative transfer between Er^{3+} dopant ions.[36] The excessive incorporation of activator ions degrades the output efficiency during laser operation. The emission intensity ratios of the first and second strongest peaks from 1535 to 1554 nm are shown in the inset of Fig. 4(b). With increasing Er^{3+} doping concentration from 0.5 to 10 at%, the ratio for the peak intensity is reduced from 1.89 to 1.18. This is assigned to severe reabsorption due to a large amount of dopants in the gain medium.[35] A simple energy diagram for the trivalent Er^{3+} ions in this study is illustrated in Fig. 4(c). Electrons can be excited from the ground state to $^4I_{11/2}$ under optical pumping at 975 nm, followed by radiative and non-radiative relaxation to $^4I_{13/2}$. Finally, the electrons emit light at a wavelength of approximately 1.5 μm due to radiative relaxation to the $^4I_{15/2}$ state.[37] The expected energy transfer from $^4I_{13/2}$ to $^4I_{15/2}$ in the Er:Y_2O_3–MgO nanocomposite at room temperature is schematically illustrated in Fig. 4(d).
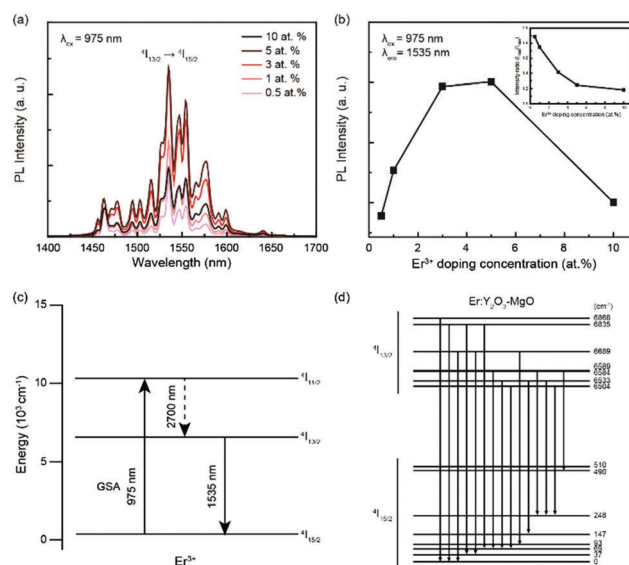
Fig. 4 Fluorescence spectra of the sintered Er:Y_2O_3–MgO nanocomposite with varying Er^{3+} doping concentrations from 0.5 to 10 at% (a) in the NIR region and (b) at 1535 nm. The inset shows the ratios of the peak intensities in the 1535 to 1554 nm wavelength range. (c) Simplified Er:Y_2O_3–MgO energy level diagram showing the laser transition at 1535 nm. (d) Experimentally measured $^4I_{15/2}$ and $^4I_{13/2}$ energy levels for the Er:Y_2O_3–MgO nanocomposite at room temperature.

The experimental identification of Stark splitting and the energy transition was realized by measuring the fluorescence spectrum, which indicates the presence of fifteen distinct emission peaks in Fig. 4(a). Notably, the diagram involves seven levels for $^4I_{13/2}$ and eight levels for $^4I_{15/2}$ based on the reference data for Er:Y$_2$O$_3$ (C$_2$ sites) although small differences exist because of the different operation temperatures.[38,39]

Absorption and emission cross-sections are important parameters used to evaluate the potential capability of laser gain media. Based on the absorption spectrum, the absorption and emission cross-sections of the 5 at% Er:Y$_2$O$_3$–MgO nanocomposite ceramics, having the strongest emission peaks, were calculated. The calculated absorption and emission cross-sections as a function of wavelength are represented in Fig. 5(a). The absorption cross-section was calculated by using eqn (1):

$$\sigma_{abs}(\lambda) = \frac{\alpha(\lambda)}{N} \tag{1}$$

where α is the absorption coefficient and N is the concentration of Er^{3+} ions per unit volume. The absorption coefficient can be calculated by the following eqn (2):[40]

$$\alpha = \frac{1}{b}\ln\left(\frac{(1-R)^2}{2T} + \sqrt{R^2 + \frac{(1-R)^4}{4T^2}}\right), \quad R = \left(\frac{n-1}{n+1}\right)^2 \tag{2}$$

where b is the thickness of the nanocomposite samples, T is the in-line transmittance and n is the refractive index of the nanocomposite that is calculated based on the Maxwell–Garnett equation.[41–43] While the maximum absorption coefficient is 4.41 cm^{-1} at 1539 nm, the background absorption coefficient is also high because of the grain boundary scattering in the near-infrared region. The absorption cross-section can be determined from normalized absorption values.[30] The maximum absorption cross-section is σ_{abs} = 3.56 × 10^{-21} cm^2 at 1539 nm. According to the McCumber theory, the stimulated emission cross-sections for the Er^{3+} ion transitions can be calculated from the absorption spectrum using the following eqn (3):[44]

$$\sigma_{ems}(\lambda) = \sigma_{abs}(\lambda)\frac{Z_l}{Z_u}\exp\left(\frac{E_0 - h\nu}{kT}\right) \tag{3}$$

where Z_l and Z_u are the lower and upper manifold partition functions, E_0 is the net free energy between the lowest levels of the two manifolds ($^4I_{15/2}$ and $^4I_{13/2}$), h is the Planck constant, k is Boltzmann's constant, and T is the temperature. The highest emission peak is located at 1544 nm with an emission cross-section of 4.07 × 10^{-21} cm^2.[30,40] To further demonstrate the potential for application as eye-safe laser gain media, the gain cross-section $\sigma_g(\lambda)$ can be calculated by the following eqn (4):

$$\sigma_g(\lambda) = \beta\sigma_{em}(\lambda) - (1-\beta)\sigma_{abs}(\lambda) \tag{4}$$

where the population inversion parameter β is the fraction of the number of Er^{3+} ions in the upper manifold compared to the total number of Er^{3+} ions. The gain cross-section values for the 5 at% Er:Y$_2$O$_3$–MgO nanocomposite are shown in Fig. 5(b). When β is greater than 0.5, the gain cross-section of the
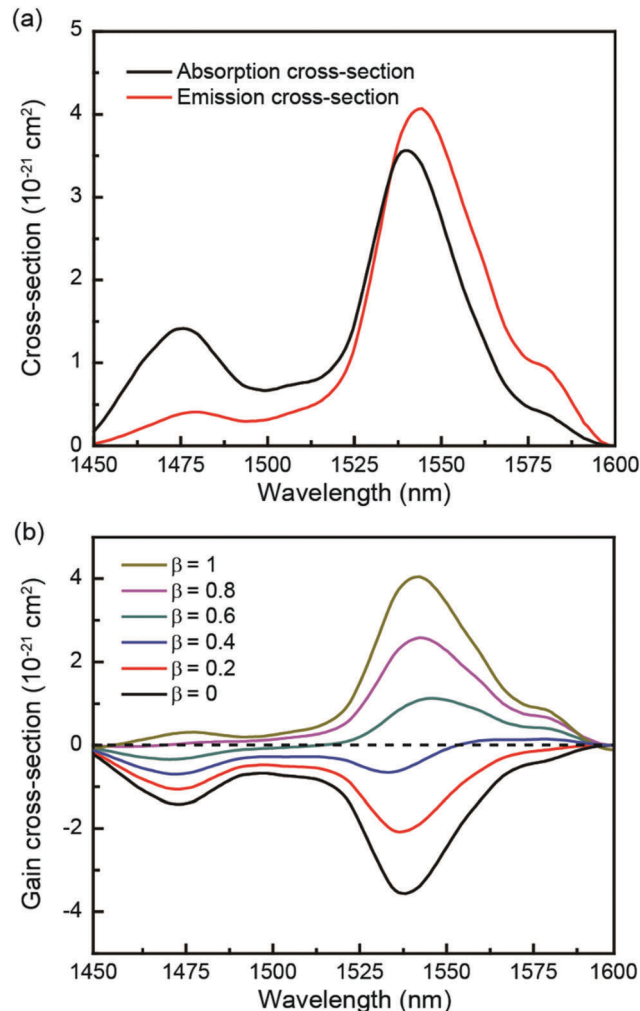
Fig. 5 (a) Absorption, emission, and (b) gain cross-section for the $^4I_{13/2} \rightarrow {^4I_{15/2}}$ transition of 5 at% Er:Y$_2$O$_3$–MgO nanocomposite ceramics. The values used for the population inversion factor are 0, 0.2, 0.4, 0.6, 0.8, and 1.

Er:Y$_2$O$_3$–MgO nanocomposite is positive at 1535 nm. This indicates that a low pumping threshold is required for laser operation.[45,46] Based on these spectroscopic analyses, it is noticeable that the Y$_2$O$_3$–MgO nanocomposite with Er^{3+} activator ions is a promising host candidate for eye-safe lasers and optical communication operating near 1535 nm.

The Vickers hardness and toughness of the Er:Y$_2$O$_3$–MgO nanocomposite with different doping concentrations were also measured. As shown in Fig. 6(a), the hardness values are approximately 10 GPa regardless of the doping concentration. This is due to the mechanical hardness being mainly dependent on the mean domain size of polycrystalline ceramics, as described by the Hall–Petch relation. As mentioned above, in the Er:Y$_2$O$_3$–MgO nanocomposite system, the difference in the ionic radius between Y^{3+} and Er^{3+} is insufficient to change the grain size. Therefore, the Er^{3+} ion doping concentration cannot affect the mechanical properties of the Y$_2$O$_3$–MgO nanocomposite gain medium. Meanwhile, the nanocomposite consists of fine grains, which can enhance the hardness through the dislocation pile-up
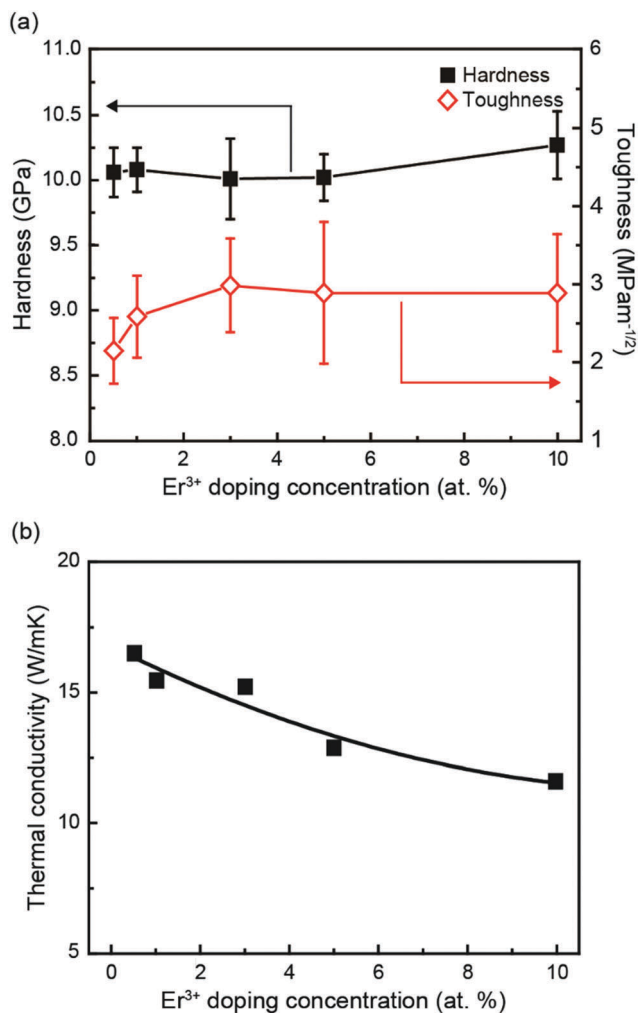
Fig. 6 (a) Hardness, toughness, and (b) thermal conductivity of the sintered Er:Y_2O_3–MgO nanocomposite with varying Er^{3+} ion dopant concentrations from 0.5 to 10 at%. The thermal conductivity was measured at room temperature.

mechanism.[47] The number of grain boundaries constitutes obstacles to dislocation movement, leading to the improved hardness.[48] The measured fracture toughnesses of the sintered samples with different Er^{3+} doping contents are shown in Fig. 6(a), with values ranging between 2 and 3 MPa m$^{-1/2}$. Thus, the fracture toughness is not dependent on the grain size.[22]

Thermal conductivity is the most crucial factor for laser ceramics since it can determine the maximum pumping density. Therefore, improvements in the thermal conductivity of gain media are essential to achieving high-power operation. The thermal conductivities of the Er:Y_2O_3–MgO nanocomposite with different Er^{3+} doping concentrations are represented in Fig. 6(b). The data show that the room temperature thermal conductivity gradually decreased from 16.49 to 11.58 W m^{-1} K^{-1} with increasing Er^{3+} doping content from 0.5 to 10 at%. Er^{3+} ions induce structural distortion in the host material. This distortion can lead to strong phonon scattering, which decreases the phonon mean free path. It can, thus, result in a deleterious effect on the thermal conductivity.[26,49] Although a large amount

of doping decreases the thermal conductivity in the Y_2O_3–MgO nanocomposite, the values for the thermal conductivity of the nanocomposite are 2 times higher than that of polycrystalline Er:Y_2O_3 at room temperature.[50] This is because of the role of the MgO phase as the main heat carrier in the nanostructure.[17] Widely used host materials including Y_2O_3 and YAG show low thermal conductivity and thermal shock resistance for high Er^{3+} ion contents. Therefore, a greatly improved thermal stability for the Y_2O_3–MgO host materials with high doping concentration can lead to the minimization of the thermal lensing effect during lasing operation that could lead to enhanced beam quality.

4. Conclusions

In this study, Y_2O_3–MgO nanocomposite ceramics doped with Er^{3+} at different doping concentrations were investigated for application as eye-safe laser gain media. We have successfully synthesized and fabricated Er:Y_2O_3–MgO nanocomposites with high doping concentrations. The Er:Y_2O_3–MgO nanocomposite shows excellent transmittance in the near and mid-infrared wavelength regions. The emission spectra for the $^4I_{13/2}$ to $^4I_{15/2}$ transition under 975 nm excitation were also recorded. Upon increasing the Er^{3+} ion doping content to 5 at%, the emission intensity increases without any observed concentration quenching. Spectroscopic analyses including measurement of the absorption, emission, and gain cross-section were carried out to demonstrate the potential use of the host material as a laser gain medium. The Er:Y_2O_3–MgO nanocomposite shows outstanding mechanical and thermal properties despite the high doping concentration, which can be used to minimize the thermal lensing effect and improve beam quality. Based on these results, we have demonstrated for the first time that an Er:Y_2O_3–MgO nanocomposite can be a promising candidate for use as an eye-safe laser host material.

Conflicts of interest

There are no conflicts to declare.

Acknowledgements

References

1 S. M. Spuler and S. D. Mayor, in *Proc. SPIE 6681, Lidar Remote Sensing for Environmental Monitoring VIII*, 2007, p. 668102.
2 J. A. Zuclich, D. A. Gagliano, F. Cheney, B. E. Stuck, H. Zwick, P. Edsall and D. J. Lund, in *Proc. SPIE 2391, Laser-Tissue interacton VI*, 1995, vol. 2391, pp. 112–125.

3 C. C. Baker, E. J. Friebele, A. A. Burdett, D. L. Rhonehouse, J. Fontana, W. Kim, S. R. Bowman, L. B. Shaw, J. Sanghera, Z. Jun, R. Pattnaik, M. DubinskiiI, J. Ballato, C. Kucera, A. Vargas, A. Hemming, N. Simakov and J. Haub, *Opt. Express*, 2017, **25**, 13903–13915.

4 Y. Li, Y. Liu, V. V. Fedorov, S. B. Mirov and Y. Wu, *Scr. Mater.*, 2016, **125**, 15–18.

5 G.-J. Zhou and W.-Y. Wong, *Chem. Soc. Rev.*, 2011, **40**, 2541.

6 G. Zhou, W. Y. Wong, S. Y. Poon, C. Ye and Z. Lin, *Adv. Funct. Mater.*, 2009, **19**, 531–544.

7 C. Yao, Z. Tian, D. Jin, Z. Feng, Y. Sun, X. Yang, G. Zhou and W.-Y. Wong, *J. Mater. Chem. C*, 2017, **5**, 11672–11682.

8 S. D. Setzler, M. P. Francis, Y. E. Young, J. R. Konves and E. P. Chicklis, *IEEE J. Sel. Top. Quantum Electron.*, 2005, **11**, 645–657.

9 E. E. Brown, U. Hömmerich, A. Bluiett, C. Kucera, J. Ballato and S. Trivedi, *J. Am. Ceram. Soc.*, 2014, **97**, 2105–2110.

10 A. a. Kaminskii, *Laser Photonics Rev.*, 2007, **1**, 93–177.

11 T. Sanamyan, J. W. Evans and S. A. McDaniel, *Opt. Express*, 2017, **25**, 16452–16457.

12 S. E. Hatch, W. F. Parsons and R. J. Weagley, *Appl. Phys. Lett.*, 1964, **5**, 153–154.

13 A. Ikesue and Y. L. Aung, *Nat. Photonics*, 2008, **2**, 721–727.

14 J. Sanghera, W. Kim, G. Villalobos, B. Shaw, C. Baker, J. Frantz, B. Sadowski and I. Aggarwal, *Materials*, 2012, **5**, 258–277.

15 S. Satapathy, A. Ahlawat, A. Paliwal, R. Singh, M. K. Singh and P. K. Gupta, *CrystEngComm*, 2014, **16**, 2723.

16 L. Zhang, Z. Huang and W. Pan, *J. Am. Ceram. Soc.*, 2015, **98**, 824–828.

17 V. L. Blair, Z. D. Fleischman, L. D. Merkle, N. Ku and C. A. Moorehead, *Appl. Opt.*, 2017, **56**, 154.

18 F. Tang, Y. Cao, J. Huang, H. Liu, W. Guo and W. Wang, *J. Am. Ceram. Soc.*, 2012, **95**, 56–59.

19 D. Fan, L.-Q. Chen and S.-P. P. Chen, *J. Am. Ceram. Soc.*, 1998, **81**, 526–532.

20 N. Moelans, B. Blanpain and P. Wollants, *Acta Mater.*, 2007, **55**, 2173–2182.

21 D. C. Harris, L. R. Cambrea, L. F. Johnson, R. T. Seaver, M. Baronowski, R. Gentilman, C. Scott Nordahl, T. Gattuso, S. Silberstein, P. Rogan, T. Hartnett, B. Zelinski, W. Sunne, E. Fest, W. Howard Poisl, C. B. Willingham, G. Turri, C. Warren, M. Bass, D. E. Zelmon and S. M. Goodrich, *J. Am. Ceram. Soc.*, 2013, **96**, 3828–3835.

22 H. J. Ma, W. K. Jung, C. Baek and D. K. Kim, *J. Eur. Ceram. Soc.*, 2017, **37**, 4902–4911.

23 X. Chen, Y. Wu, N. Wei, J. Qi, Y. Li, Q. Zhang, T. Hua, W. Zhang, Z. Lu, B. Ma and T. Lu, *J. Lumin.*, 2017, **188**, 533–540.

24 H. Birol, C. Renato Rambo, M. Guiotoku and D. Hotza, *RSC Adv.*, 2013, **3**, 2873.

25 S. H. Jo, J. H. Kim and D. K. Kim, *Mater. Sci. Forum*, 2007, **539–543**, 1373–1378.

26 L. Zhang and W. Pan, *J. Am. Ceram. Soc.*, 2015, **98**, 3326–3331.

27 W. K. Jung, H. J. Ma, S. W. Jung and D. K. Kim, *J. Am. Ceram. Soc.*, 2017, **100**, 1876–1884.

28 Y. Sun, Q. Yang, H. Wang and Y. Shao, *J. Lumin.*, 2018, **194**, 50–55.

29 J. B. Gruber, K. L. Nash, D. K. Sardar, U. V. Valiev, N. Ter-Gabrielyan and L. D. Merkle, *J. Appl. Phys.*, 2008, **104**, 23101.

30 C. Li, T. Xie, Z. Ye, B. Yao, H. Kou, Y. Pan and J. Li, *J. Am. Ceram. Soc.*, 2017, **100**, 2081–2087.

31 E. H. Penilla, L. F. Devia-Cruz, M. A. Duarte, C. L. Hardin, Y. Kodera and J. E. Garay, *Light: Sci. Appl.*, 2018, **7**, 33.

32 L. L. Zhu, Y. J. Park, L. Gan, S. Il Go, H. N. Kim, J. M. Kim and J. W. Ko, *Ceram. Int.*, 2017, **43**, 13127–13132.

33 D. K. Sardar, K. L. Nash, R. M. Yow and J. B. Gruber, *J. Appl. Phys.*, 2007, **101**, 1–5.

34 J. Liu, Q. Liu, J. Li, M. Ivanov, X. Ba, Y. Yuan, L. Lin, M. Chen, W. Liu, H. Kou, Y. Shi, H. Chen, Y. Pan, X. Cheng and J. Guo, *Opt. Mater.*, 2014, **37**, 706–713.

35 N. Jaba, M. Ajroud, G. Panczer, M. Férid and H. Maaref, *Opt. Mater.*, 2010, **32**, 479–483.

36 I. C. Robin, R. Kumaran, S. Penson, S. E. Webster, T. Tiedje and A. Oleinik, *Opt. Mater.*, 2008, **30**, 835–838.

37 Y. Jiang, J. Fan, B. Jiang, X. Mao, J. Tang, Y. Xu, S. Dai and L. Zhang, *Sci. Rep.*, 2016, **6**, 29873.

38 N. C. Chang, J. B. Gruber, R. P. Leavitt and C. A. Morrison, *J. Chem. Phys.*, 1982, **76**, 3877.

39 L. D. Merkle and N. Ter-Gabrielyan, *J. Lumin.*, 2013, **133**, 254–256.

40 G. N. van den Hoven, J. A. van der Elsken, A. Polman, C. Van van Dam, K. W. van Uffelen and M. K. Smit, *Appl. Opt.*, 1997, **36**, 3338–3441.

41 M. Jonasz and G. Fournier, *Light Scattering by Particles in Water: Theoretical and Experimental Foundations*, Elsevier Science, 2011.

42 R. E. Stephens and I. H. Malitson, *J. Res. Natl. Bur. Stand.*, 1934, **1952**(49), 249.

43 Y. Nigara, *Jpn. J. Appl. Phys.*, 1968, **7**, 404.

44 D. E. McCumber, *Phys. Rev.*, 1964, **134**, 299.

45 F. Chen, T. Wei, X. Jing, Y. Tian, J. Zhang and S. Xu, *Sci. Rep.*, 2015, **5**, 10676.

46 U. Hömmerich, C. Hanley, E. Brown, S. B. Trivedi and J. M. Zavada, *J. Alloys Compd.*, 2009, **488**, 624–627.

47 I. McColm, *Ceramic Hardness*, Springer Science & Business Media, 2013.

48 K. Morita, B. Kim, K. Hiraga and H. Yoshida, *J. Mater. Res.*, 2009, **24**, 2863.

49 F. Tang, W. Wang, X. Yuan, C. Zhu, J. Huang, C. Ma, F. Wang, Y. Lin and Y. Cao, *J. Alloys Compd.*, 2014, **593**, 123–127.

50 T. Sanamyan and Z. Fleischman, in *Proc. SPIE 9466, Laser Technology for Defense and Security XI*, 2015, p. 94660I.

This journal is © The Royal Society of Chemistry 2018

J. Mater. Chem. C, 2018, **6**, 11096–11103 | **11103**